# Nanotopographic Control of Actin Waves and Growth Cone Navigation in Developing Neurons

Spandan Pathak, Kate M. O'Neill, Emily K. Robinson, Matt J. Hourwitz, Corey Herr, John T. Fourkas, Edward Giniger, Wolfgang Losert

## Abstract

The development of axons and dendrites (neurites) in a neural circuit relies on the dynamic interplay of cytoskeletal components, especially actin, and the integration of diverse environmental cues. Building on prior findings that actin dynamics can serve as a primary sensor of physical guidance cues, this work investigates the role of nanotopography in modulating and guiding actin waves and neurite-tip dynamics during early neural circuit development. Although actin dynamics is well known to contribute to pathfinding in wide axonal tips, typically referred to as growth cones, we also observe dynamic actin remodeling throughout neurites and at other, narrower, neurite tips. We find that actin-wave speeds do not change significantly in the first two weeks of neurite development on flat substrates, but decrease over the same period in neurites on nanoridges. The ability of nanoridges to guide actin waves and the neurite-tip direction also decreases as neurites mature, both for narrow tips and wide growth cones. This change in responsiveness to physical guidance cues with neuronal maturation may impact the regenerative capacity of developing neural cells that are inserted into mature brains.

## 1. Introduction

The development of a functional nervous system is a marvel of Nature, relying on the precise navigation and connection of countless neurons. This intricate process of neural circuit formation relies on the dynamic behavior of developing neurons that extend neurites – projections that will ultimately become axons and dendrites (1, 2). This navigation depends critically on the active and tightly regulated remodeling of the actin cytoskeleton (3, 4). Actin filaments (F-actin), in conjunction with microtubules (5, 6), underlie the extension and steering of axons, as well as synapse formation (7).

Although growth-cone-led axonal development has been studied widely, recent work has shown that cytoskeletal dynamics may also direct growth for narrow neurite tips (8, 9). It was demonstrated recently, for example, that in the *Drosophila* wing disc, the tip of the pioneer neuron TSM1 is almost exclusively narrow and filopodial (10). In this case, genes for proteins such as Abelson tyrosine kinase regulate actin organization and, therefore, the advance of the axonal tip (10, 11) through actin dynamics that occurs distant from the leading edge. Neurons also seem to possess mechanisms to regulate neurite elongation that act in regions other than the growth cones. For example, differential neurite growth, including the selection of a single axon during initial polarization and the alternating growth of axon branches, occurs even in the absence of growth-cone motility (12). This observation suggests that neurons possess mechanisms for local regulation of neurite elongation in regions other than the growth cones.

Further, although the actin waves that traverse the length of the axon are associated with growth and retraction, conflicting views have emerged regarding the precise roles of these waves. On the one hand, neurite elongation, which may reach hundreds of microns, can occur independently of actin waves (13). Conversely, other studies have shown that, during early neuronal development, actin waves drive fluctuations in neurite outgrowth by controlling microtubule transport (14). In some cases, competition among neurites, which is mediated by actin waves, is proposed to allow the neuron to explore its environment until external cues specify the axon (15). These findings suggest that actin waves act more as passive responders to stochastic internal forces rather than as active drivers of axon extension and growth-cone formation.

Classic studies of axon patterning, such as those described above, have largely focused on what happens inside the axon and growth cone. However, the physical properties of the microenvironment, such as substrate stiffness (16) and topography, also can exert a profound influence on neuronal growth behavior in different stages of development (17, 18). In early stages (4 to 20 hours post plating), specific topographic cues can direct neuronal polarization by attracting key markers, resulting in preferential axon growth along micropatterned features (19). With further development (4 to 5 days post plating), growth cones on such substrates became more elongated and aligned with respect to the neurite shaft (20). These findings highlight the importance of considering the three-dimensional complexity of the *in vivo* environment when studying the role of actin dynamics in axonal guidance and growth-cone navigation.

The current work investigates the role of nanoridges in modulating actin waves in neurites and growth cones during neuronal development. We examine the speed of actin waves and the guidance of actin waves, neurites, and growth cones by the topography of the microenvironment. Because actin waves have been identified as primary sensors of the physical microenvironment, including electric fields (21) and texture (22, 23), our work also sheds light on whether neuronal development also alters the ability of cells to sense their physical environment.

## 2. Materials and Methods

### 2.1 Primary neuronal dissections and cell culture

Primary neurons were obtained from Sprague Dawley rats housed at the University of Maryland (with approval by the University of Maryland Institutional Animal Care and Use Committee; protocols R-JAN-18-05 and R-FEB-21-04). At embryonic day of gestation 18 (E18), primary cortical neurons were obtained via dissection, and were cultured as previously described (24). We did not distinguish between cortices from male and female embryos. Briefly, hippocampi and cortices were dissected from decapitated embryos. Cortices from all embryos were combined and triturated manually, and then were counted using a hemocytometer. A monolayer of cortical neurons was plated in 35-mm imaging dishes with glass centers (cat. no. P35G-1.5-20-C, MATTEK) at a density of $5 \times 10^5$ cells per dish (520 cells/mm$^2$). Prior to the plating, the imaging dishes were coated with 0.1 mg/mL poly-D-lysine (PDL; cat. no. P0899, MilliporeSigma) for at least 1 h at 37 °C and then were washed three times with phosphate buffered saline (PBS; cat. no. SH30256.01, Cytiva). Monolayers were also plated on acrylic nanoridges, which received the following treatments prior to neuronal plating: soaking in ethanol (24 h), followed by soaking in media (24 h), followed by PDL coating (24 h), and finally 10 μg/ml laminin coating (24 h; cat. no. L2020, MilliporeSigma), all at 37 °C. Cultures were maintained in NbActiv4 medium (cat. no. Nb4-

500, BrainBits) supplemented with 1% penicillin/streptomycin (P/S; cat. no. 15070063, Thermo Fisher Scientific) at 37 °C in 5% $CO_2$. Half of the medium was changed twice per week. Please note that we did not optimize the nanoridges for longer term neuronal survival (DIV14+), which is why our data for cells on nanoridges are only reported at the early and middle developmental stages.

### 2.2 Transduction with Actin-GFP

For visualization of actin dynamics within primary cortical neurons, we used CellLight Actin-GFP, BacMam 2.0 (cat. no. C10506, ThermoFisher Scientific). This viral vector has low toxicity and labels cells sparsely. Given that neurons have complex morphological structures even in early stages of development, the latter feature is particularly helpful for analysis of single-cell actin dynamics. At 48 to 72 h prior to imaging, 5 to 10 µL of CellLight was mixed with the cell culture medium (1 to 2 particles per cell; PPC). The medium was fully changed approximately 20 h after transduction, and imaging was performed 24 to 48 h later.

### 2.3 Confocal imaging

Live-cell imaging of primary cortical actin dynamics was performed at the University of Maryland Imaging Core using a PerkinElmer spinning-disk confocal microscope. For all experiments, we used an oil-immersion, 40× objective (1.30 NA; 0.36 µm/pixel), and maintained live cultures under temperature, humidity, and $CO_2$ control. We recorded 16-bit images using a Hamamatsu ImagEM X2 EM-CCD camera (C9100-23B) and acquired time-lapse images with PerkinElmer's Volocity software (version 6.4.0). We identified transduced neurons via a positive signal in the 488-nm laser channel. We performed imaging in growth media and acquired images every 2 s in the 488-nm channel for 5 to 10 min. We ensured a consistent *z*-plane with Perfect Focus (Nikon PFS).

### 2.4 Preparation of nanotopographic surfaces (nanoridges)

Nanoridge substrates for the neuronal experiments featured the same master pattern as in a recent study that focused on the photomodification and reshaping of nanotopographic structures (25). Briefly, a large-scale pattern with 750-nm high, 400-nm wide nanoridges at a 3.2-µm pitch (25), initially fabricated on a silicon wafer using interference lithography, was replicated using soft lithographic techniques, as described in more detail elsewhere (26) to produce a polydimethylsiloxane (PDMS) mold with negative relief of the master pattern. Molding of the patterned silicon wafer was facilitated by exposure to plasma treatment in an oxygen atmosphere and subsequent surface functionalization of the wafer with (tridecafluoro-1,1,2,2-tetrahydrooctyl)methyldichlorosilane (Gelest, CAS #: 73609-36-6) under vacuum inside a desiccator. These steps reduce the surface energy of the wafer to prevent adhesion with the PDMS during the molding process. A hard PDMS layer was spin-coated onto the pattern and Sylgard 184 (Dow) comprised the remainder of the mold (27). The mold was peeled from the master after several baking steps. Replicas of the original pattern were then produced using nanoimprint lithography. A photocurable resin was prepared using a 1:1 w/w mixture of ethoxylated(6)trimethylolpropane triacrylate (Sartomer, CAS #: 28961-43-5) and tris (2-hydroxy ethyl) isocyanurate triacrylate (Sartomer, CAS #: 40220-08-04), and 3 wt% of the photoinitiator

Irgacure TPO-L (BASF, CAS #: 84434-11-7). Glass coverslips featuring pendant acrylate groups were produced by plasma treatment under oxygen for 3 min followed by stirring in a 2% solution of (3-acryloxypropyl)trimethoxysilane (Gelest, CAS #: 4369-14-6) for at least 12 h. A drop of the resin was sandwiched between the PDMS mold and an acrylated coverslip, and then was exposed to UV light for 5 min to transfer the pattern to the photoresist. The patterned coverslip was then detached from the mold.

### 2.5 Image Analysis

**Determination of actin-flow vectors using optical flow:**

Image-registration and intensity-adjustment functions within the `scikit-image` module (Python) were used to correct jitter and photobleaching, respectively, in the raw videos. To remove random background noise, processed videos were smoothed in time using a Gaussian-like filter across five successive frames (28). The smoothing timescale was considerably shorter than the timescale at which actin-wave motion is discernible. Subsequently, optical flow was performed on the smoothed image frames using the Lucas-Kanade method (29). A Gaussian weighting matrix ($\sigma$ = 2 pixels = 0.72 μm) was applied around each pixel location to extract local flow vectors. A reliability threshold of 0.1 was used to remove noisy flow vectors. We validated that the choice of the Gaussian-filter parameters (size and shape), and we ensured that modest changes in the reliability threshold did not significantly influence motion capture or downstream analysis.

**Neuronal masking:**

`Scikit-image` (Python) functions were used for the generation and refinement of binary masks. Mean frames were generated, and low-contrast frames were processed using contrast-limited adaptive histogram equalization. A white top-hat filter (with a disk-shaped structuring element of radius = 15 pixels = 5.4 μm) was applied to highlight darker neuronal processes. Adaptive local thresholding (the Niblack method (30)) yielded an initial binary mask, which was refined by multiple iterative morphological opening steps, retaining the *n* largest connected components after manual review and background-noise exclusion. Subsequently, manual selection of a region corresponding to the cell body was employed due to the inherent lack of consistent alignment of the cell bodies. This approach enabled the isolation of neuronal processes from the larger cell mask, and ensured that subsequent analyses focused on the dynamic behavior of actin within the neurites. Neuronal process orientation was determined using a rotating Laplacian-of-Gaussian filter on the mean image-frame (31).

**Clustering of optical-flow vectors:**

Optical-flow vectors were clustered locally by spatially averaging the flow vectors. A Gaussian neighborhood (11 × 11 matrix with $\sigma$ = 5 pixels = 1.8 μm) was used to assess vector alignment by calculating the dot product between vectors and their corresponding neighborhood (32). Cluster peaks were detected with the `trackpy` (Python) module using an approximate detection diameter of 5 pixels = 1.81 μm and a minimum separation of 15 pixels = 5.4 μm between two neighboring peaks. Detected particle positions for each frame were stored and were subsequently linked across frames to form trajectories with a search range of 5 pixels = 1.8 μm between successive frames and a memory of one frame (2 s), enabling cluster-track analysis. To emphasize longer-scale actin flows, only tracks persisting for at least eight frames (14 s) were analyzed. We calculated and stored per-frame and per-track metrics, including instantaneous

shifts, displacement, velocity, movement angle, track length, duration, net distance, average velocity, average speed and sinuosity. To exclude static clusters, only tracks with an average instantaneous speed greater than 0.5 pixels/frame = 5.4 μm/min were retained.

**Growth-cone orientation:**

Growth-cone boundaries were identified manually and extracted using ImageJ. The alignment of the central shaft was then determined by identifying its major axis.

**Wasserstein distance:**

The Wasserstein distance ($W_1$) was used to quantify the dissimilarity between two probability distribution functions (PDF) (33). This metric represents the area between the corresponding cumulative distribution functions (CDFs). Mathematically, for two probability measures $\mu$ and $v$ on the real line with CDFs $F$ and $G$, respectively, the Wasserstein distance ($W_1$) is defined as $W_1(\mu, v) = \int |F(x) - G(x)|\, dx$. The Wasserstein distance is a useful tool for quantifying modest changes in broad distributions.

**Pooling of DIV (days *in vitro* after plating) videos and statistical testing:**

For dynamics analysis, on flat surfaces we categorized videos from DIV 2 to 5 as 'early' ($N$ = 17), from DIV 7 to 12 as 'middle' ($N$ = 21), and from DIV 14 to 23 as 'late' ($N$ = 17) developmental stages. On nanoridges, DIV 2 to 4 were grouped as 'early-stage' ($N$ = 9), and DIV 7 to 8 as 'middle-stage' ($N$ = 6).

To compare multiple independent test groups, we first performed the Shapiro-Wilk test to assess normality (34). If the data met the assumption of normality, we conducted a one-way ANOVA to test for overall group differences, followed by Tukey's *post hoc* test to determine which group means differed significantly (35). For data that did not meet normality assumptions, we used the Kruskal-Wallis test instead (36), followed by Dunn's *post hoc* test for pairwise comparisons (37). For comparisons between two groups, we used the *t*-test (38) when both groups passed the normality test (34), and the Mann-Whitney U test when either or both groups did not pass the normality test (39).

## 3. Results

## Actin dynamics is persistent throughout different stages of development on both flat and nanoridged surfaces

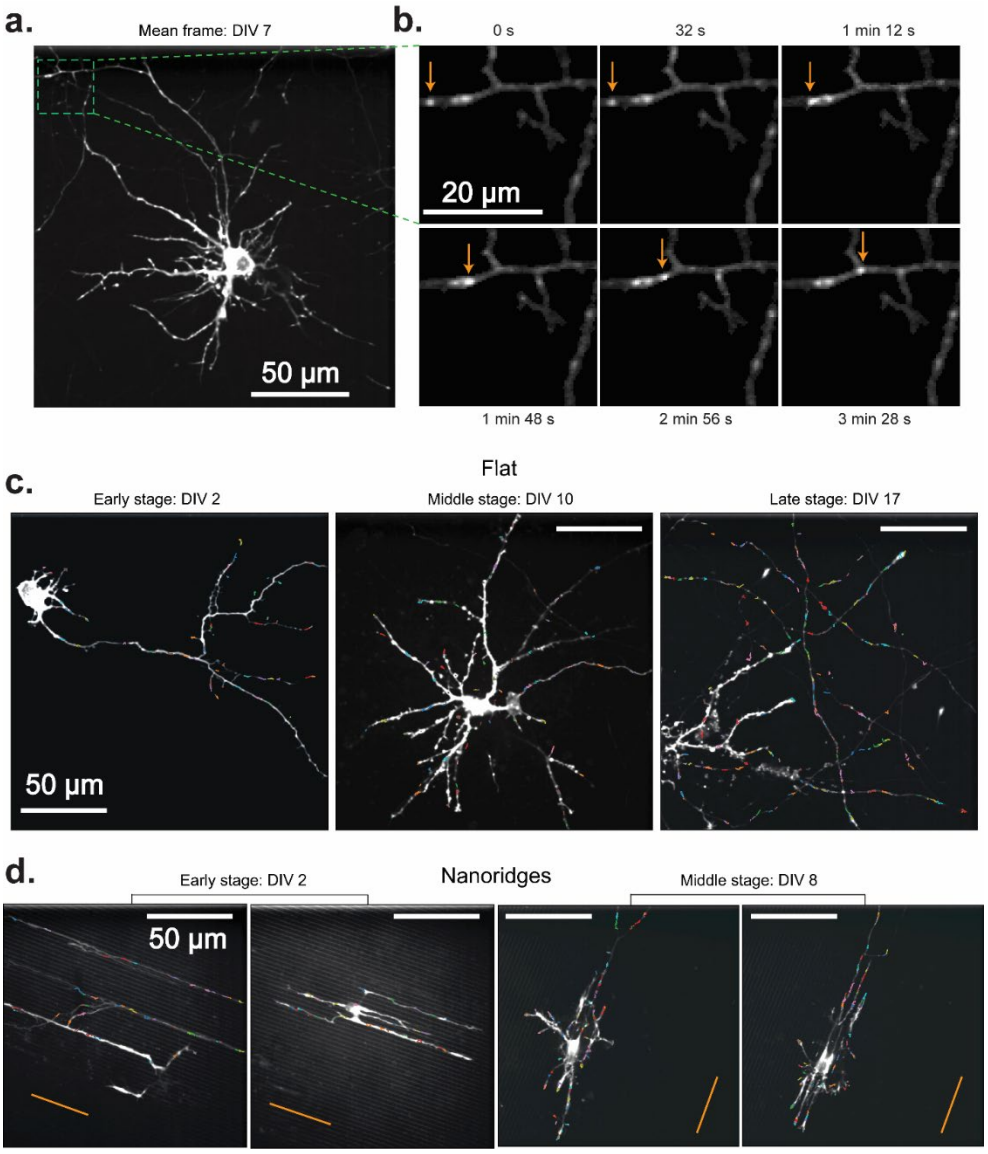


**Figure 1. Actin waves in primary rat cortical neurons in different DIV stages on flat and nanoridged surfaces.** (a) Mean image of a representative DIV 7 neuron cultured on a flat surface. The green box indicates a region of interest, which is shown in a magnified version in (b). (b) The trajectory of an actin wave (orange arrows) moving along a neuronal process. Actin tracks overlaid from representative videos, color-coded by individual track, for each developmental stage on (c) flat surfaces and (d) 3.2-µm-spaced nanoridges. On flat surfaces, the imaging durations were 5 min, 4 min 10 s and 8 min, respectively, for the representative videos from early, middle and late developmental stages. On nanoridges, the imaging durations were 5 min, 5 min, 10 min and 10 min, respectively, for the representative videos from early, early, middle and middle developmental stages. The orange lines indicate the nanoridge alignment.

Figure 1 illustrates the cluster-tracking workflow's ability to capture localized actin-wave dynamics at a range of neuronal developmental stages on both flat and nanoridged substrates. A

representative mean-image frame derived from a video on a flat surface (Fig. 1a-b) reveals perceptible actin flow, as characterized by a moving bright spot (orange arrows). The transient nature of these actin movements is indicated by the cluster tracks presented in Fig. 1c-d. Notably, these tracks exhibit a predominantly localized spatial distribution, and frequently display back-and-forth motion, lacking a clear, sustained directional bias. Furthermore, a discernible correlation is observed between the track alignment and the underlying neuronal processes, suggesting a potential guidance mechanism. These dynamic actin tracks are observed in early-, middle-, and late-stage neurons cultured on flat surfaces (Fig. 1c), as well as in early- and middle-stage neurons cultured on nanoridged surfaces (Fig. 1d). The consistent observation of localized, dynamic actin movements at different developmental stages on flat and nanoridged substrates underscores the persistent and adaptable nature of actin dynamics in neuronal development.

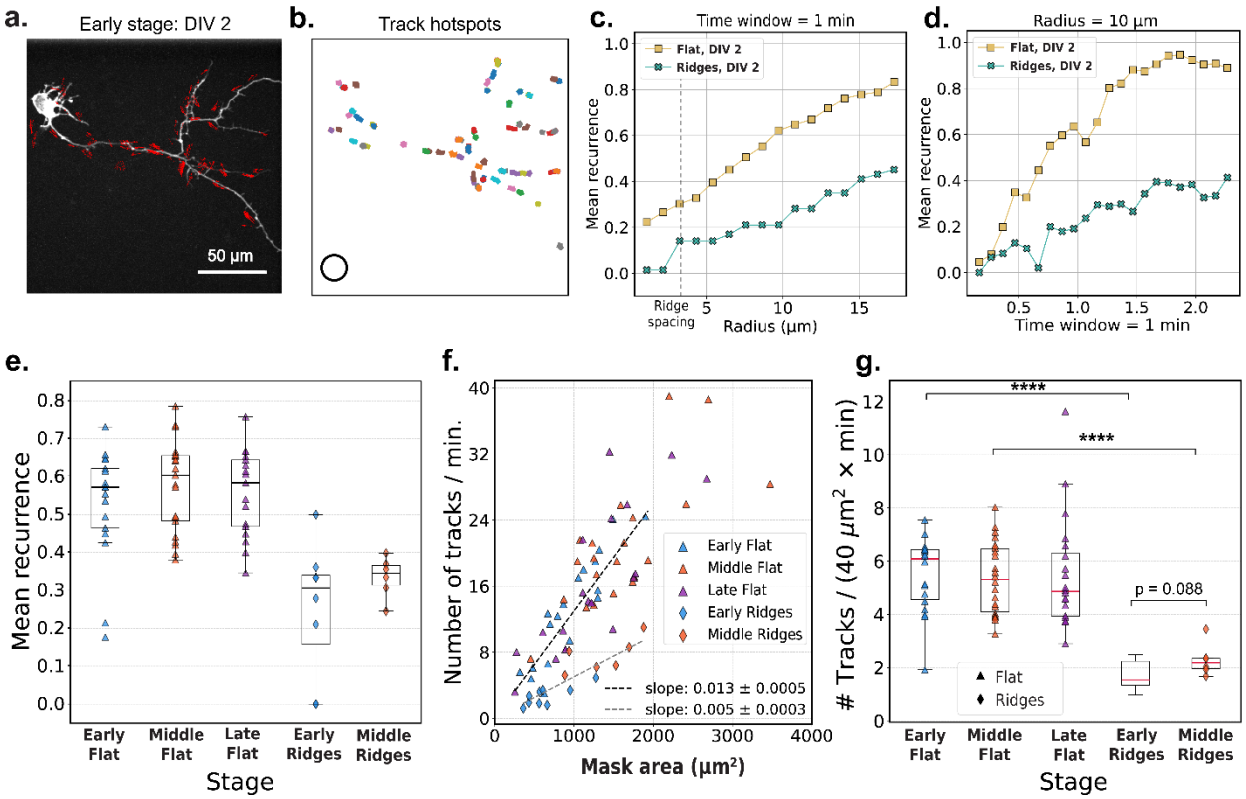


**Figure 2. Actin-track dynamics and recurrence depend on the microenvironment.** (a) Representative image frame with optical-flow vectors for a DIV2 neuron cultured on a flat surface. (b) Actin tracks observed over a 5-min interval from the same video as in (a). The circle illustrates the 10 µm search radius used to compute mean recurrence values shown in panels (d) and (e). (c-d) Mean recurrence quantifies the fraction of new actin tracks originating within a circular region during each time window. Mean recurrence as a function of (c) radius (with a 1-min time window) and (d) time window (at a fixed search radius of 10 µm) for two representative early-stage videos on flat and nanoridged substrates. (e) The mean recurrence for early ($N$ = 17), middle ($N$ = 21), and late ($N$ = 17) videos, respectively, on a flat substrate and for early ($N$ = 9) and middle ($N$ = 6) videos, respectively, on nanoridged substrates. (f) Tracks/min plotted as a function of the neuronal mask area (excluding the cell body) with linear fits (through origin) for flat ($N$ = 55) and nanoridged substrates ($N$ = 15). (g) Normalized track counts at different developmental stages. For (e)-(g), each scatter point corresponds to a unique video. Statistical tests were performed on pooled data.

Significance is reported as $p$-value for $0.1 > p > 0.05$, * for $p \leq 0.05$, ** for $p \leq 0.01$, *** for $p \leq 0.001$, and **** for $p \leq 0.0001$.

Figure 2 quantifies the total number and spatial distribution of localized actin tracks within neuronal processes. Figure 2a shows representative optical-flow vectors from a selected time frame. These flow vectors were clustered in space and time to form robust actin tracks (Fig. 2b). Mean recurrence was defined as the fraction of actin tracks originating in the same spatial region in successive time windows. Figures 2c and 2d explore how the mean recurrence varies as a function of spatial search radius and temporal window size, respectively. Figure 2e shows mean-recurrence values compared on flat and nanoridges substrates. Shapiro-Wilk tests indicated that all groups followed a normal distribution except for the early-stage group on a flat substrate ($p$ = 0.0293), so non-parametric tests were used in this case. Mann-Whitney U tests showed that the cells on the nanoridges had significantly lower mean recurrence than on the flat substrates at both the early ($p$ = 0.00222) and middle ($p = 2.7 \times 10^{-5}$) stages. However, comparisons at different developmental stages for the same substrate revealed no significant differences (flat substrates $p$ = 0.70, nanoridges $p$ = 0.271).

Figure 2f shows that there is a linear relationship between the tracks/min and the neuronal mask area, with data from cells on nanoridges exhibiting a shallower slope (0.005) than those on a flat substrate (0.013). Shapiro-Wilk tests confirmed that all groups exhibited normal distributions except for the late-stage data on flat substrates ($p$ = 0.008), which deviated from normality (Fig. 2g). Mann-Whitney U tests showed that cells on nanoridges had significantly lower normalized track counts than cells on flat substrates at both the early ($p = 6.7 \times 10^{-5}$) and middle ($p = 1.1 \times 10^{-5}$) developmental stages. However, comparisons for a single substrate type at different developmental stages (early vs. middle vs. late on flat substrates and early vs. middle on nanoridges) revealed no significant differences ($p$ = 0.67 and $p$ = 0.088, respectively), again suggesting that topographical surface exerts a stronger influence on actin dynamics than does the developmental stage.

Taken together, these results demonstrate both less frequent initiation of actin waves and less overall actin activity on the nanoridges. Next, we examined whether wave speed is also affected by the nature of the substrate.

## Actin-wave-speeds

Figure 3 illustrates how the distribution of actin-wave speeds depends on the developmental stage and on flat vs. nanoridged substrates. Figure 3a is a representative actin time-lapse image for a DIV8 neuron on a nanoridged surface. The inset highlights an active growth cone, with brightly colored regions indicating intense actin activity over a 10-min period. Figures 3b captures the growth cone's retraction, which is followed by a slower forward extension. This alternating motion is characteristic of growth-cone-guided actin waves. In this example, the growth cone moves parallel to the underlying ridges. To examine localized dynamics on short time scales, we analyzed instantaneous actin speeds. On flat surfaces (Fig. 3c), the speed distributions were similar for the early, middle, and late developmental stages, with a mean speed of roughly 21 μm/min. However, on nanoridged surfaces (Fig. 3d), a ~10% decrease in wave speed was observed when going from the early to the middle developmental stage. We quantified differences between individual

experiments using the Wasserstein distance ($W_1$). We found that the $W_1$ metric between median CDFs was higher for the early vs. the middle stage on nanoridges as compared to on flat surfaces between any two developmental stages. These findings indicate that neuronal maturation slows actin-wave propagation to some extent on nanoridged substrates, but has little effect on flat surfaces. It is possible that the differential effects on speed observed on flat vs. nanoridged substrates are related to the more physiologically-relevant environment of the nanoridged substrates.

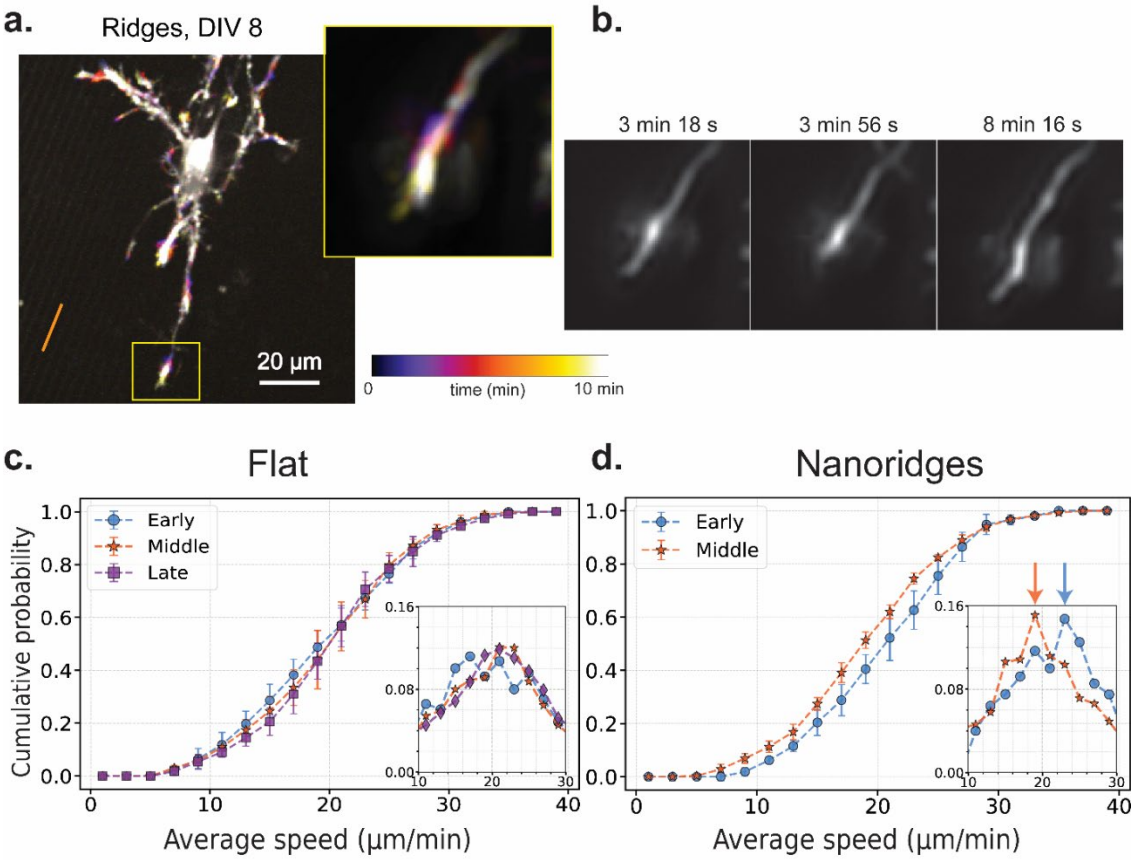


**Figure 3. Actin-wave speed as a function of developmental stage and substrate identity.** (a) A representative actin time-lapse image of a DIV8 neuron on a nanoridged surface. The inset shows a highly active growth cone over a 10-min period. The orange line indicates the nanoridge alignment. (b) The growth-cone trajectory from the same time-lapse image, showing alternating retraction and forward extension along the ridge direction. We applied the AI-based model ZS-DeconvNet (40) to denoise individual frames, exclusively for visualization purposes. (c) CDF of the average wave speed for neurons cultured on flat surfaces for the three different developmental stages ($N$ = 17, 21, 17 for the early, middle and late stages, respectively). (d) CDF of the average wave speed for neurons cultured on nanoridged surfaces for the early ($N$ = 9) and middle ($N$ = 6) developmental stages. In (c) and (d), the insets show the corresponding probability distribution function (PDF) near the peak. Number of bins = 20. The arrows in (d) point to the corresponding distributions' median values. The error bars represent the interquartile range of the CDF at each bin across all videos for each condition, and the markers indicate the corresponding median values. For each pair of conditions, we calculated the Wasserstein Distance ($W_1$) between the median CDFs, as well as the maximum and minimum distances among all combinations of 25th and 75th percentile CDFs. These are reported in the format: median (minimum to maximum). On flat surfaces, the $W_1$ values were 0.53 (0.43 to 2.56) for early vs. middle, 0.54 (0.61 to 2.84) for middle vs. late, and 0.82 (0.66 to 2.91) for

early vs. late stages. On nanoridges, the $W_1$ value between early and middle-stage neurons was 1.59 (0.76 to 3.36).

## Cellular processes align actin waves more effectively than do nanoridges

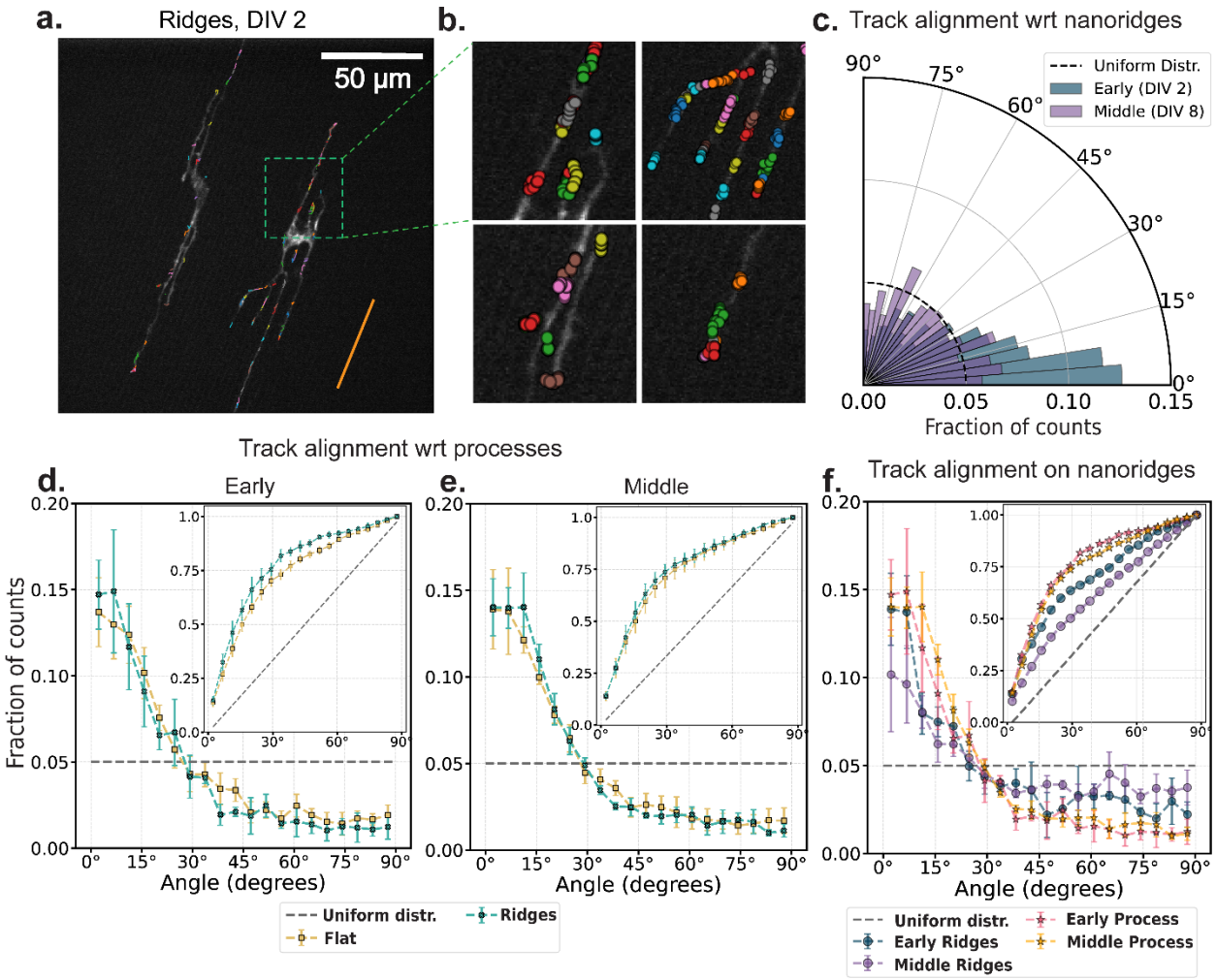


**Figure 4. The influence of nanotopography and developmental stage on actin-track alignment.** (a) Actin-cluster tracks accumulated for 10 min for a DIV2 neuron on nanoridges. The orange line indicates the nanoridge alignment. (b) Zoomed-in view of selected regions with actin tracks. (c) Alignment of actin tracks with respect to the nanoridges for two representative videos from early (DIV 2) and middle (DIV 8) developmental stages. The dashed line represents a uniform distribution of track alignments for the same bin size. There are 20 bins. (d, e) Fraction of track segments aligned at various angles with respect to neuronal processes on flat and nanoridged surfaces, at the (d) early and (e) middle developmental stages. (f) Relative alignment of track segments on nanoridges with respect to neuronal processes and the nanoridge for the early and middle developmental stages. The error bars represent the interquartile range of the CDF at each bin across all videos for each condition, and the markers indicate the corresponding median values. From (d-f), the insets show the corresponding CDF. For each pair of conditions, we calculated the Wasserstein Distance ($W_1$) between the median CDFs and the maximum and

minimum distances among all combinations of 25th and 75th percentile CDFs. These values are reported in the format: median (minimum to maximum). For early (c) and middle (d) stage neurons, the $W_1$ value between flat and ridge surface movies were 3.91 (1.42 to 7.07) and 1.39 (1.34 to 7.03) respectively. On nanoridges, for early and middle stage neurons, $W_1$ value between ridge and process guidance CDFs were 6.80 (3.0 to 13.5) and 12.07 (6.12 to 20.45) respectively. For process and ridge guidance comparisons, in early vs middle stage movies, the $W_1$ values were 2.12 (1.16 to 5.96) and 7.23 (1.64 to 14.83), respectively.

In Fig. 4 we analyze the influence of nanoridges and neuronal processes on actin-track alignment at different developmental stages. In Fig. 4a, tracks of actin clusters accumulated over 10 min indicate the propensity of the tracks to follow the nanoridge direction. Zoomed-in views of selected regions (Fig. 4b) further indicate the linearity of tracks, and show that the neuronal processes also tend to be aligned with the nanoridges. The bias towards actin-track alignment with the nanoridges is quantified in Fig. 4c. Although we find most of the tracks to be aligned with the nanoridges, there is also a developmental-stage effect on this alignment: there is less alignment in the representative video at the middle stage than in the representative video in the early stage.

We next explore the alignment of actin tracks with respect to the direction of the neural process in which they reside. At the early (Fig. 4d) and middle (Fig. 4e) developmental stages, actin tracks remain strongly aligned with their respective processes, regardless of whether the neurons are cultured on flat or nanoridged substrates. A comparison of early and middle developmental stage videos on nanoridges (Fig. 4f) shows a clear decrease in the alignment of actin tracks on nanoridges as development progresses, whereas the alignment with the processes remains relatively unchanged. Moreover, the inset in Fig. 4f shows that alignment with the neuronal processes consistently exceeds alignment with the nanoridges, suggesting the idea that dynamic intracellular cues, such as membrane tension or cytoskeletal reorganization, play a more dominant role in steering actin dynamics over time than does static external topography.

It is important to note that at early stages of development, the neuronal processes themselves are closely aligned with the nanoridges. This initial bias could give the impression that nanoridges directly guide actin dynamics, when in fact the processes may serve as the intermediate conduit. As development progresses, and the processes start diverging from the ridge direction, the decreasing alignment between actin tracks and nanoridges becomes more apparent. This observation raises a fundamental question: to what extent is actin guidance influenced by the internal architecture of the cell versus the external physical environment? Or is it the physical environment that guides the intracellular cues, and thus the actin dynamics of growing neurite tips, in a self-evolving feedback loop?

## Impact of nanoridges on growth-cone alignment

To explore the contributions of internal vs. external physical cues to cytoskeletal guidance, we next consider the structural features of developing growth cones. Specifically, we analyzed how the growth-cone alignment is related to nanoridge orientation throughout development. Figures 5a and 5b show representative examples of growth cones oriented parallel (at DIV 2) and perpendicular (at DIV 8) to the nanoridges. Notably, the perpendicular growth cone in Fig. 5b (green box) originates from a neighboring neuron outside the field of view, and appears at the end of a neurite that spans multiple ridges. Figure 5c shows the growth-cone alignment as a function

of growth-cone width, and reveals a developmental trend. Early-stage neurons (shown in darker shades) exhibit a strong preference for alignment with the nanoridges. This preference diminishes at later stages.

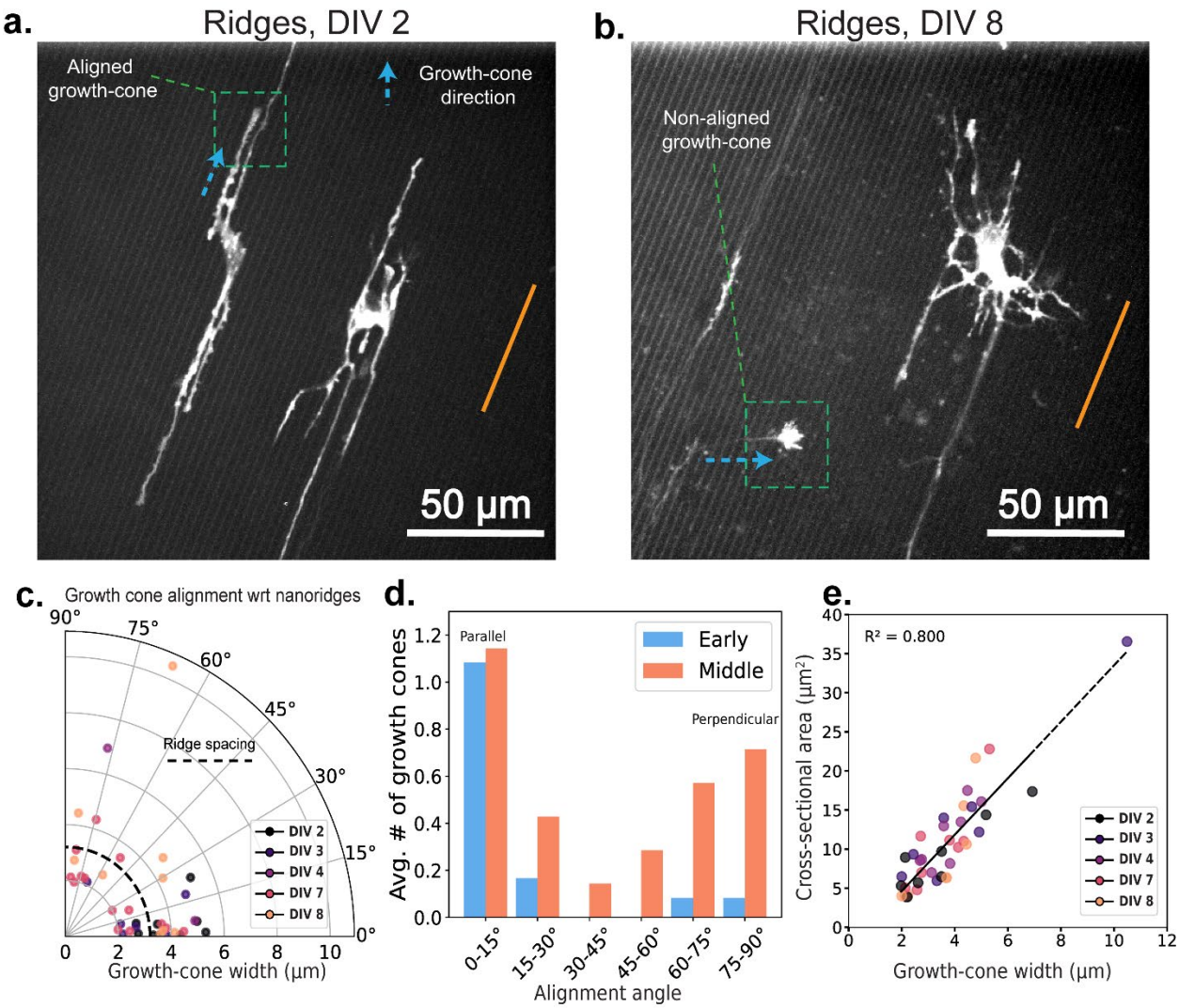


**Figure 5. Growth-cone orientations at different developmental stages for neurons on nanoridges.** Representative growth cones oriented (a) parallel to (DIV 2) and (b) perpendicular to (DIV 8) the nanoridges. The nanoridge directions are indicated by orange lines, and the growth-cone orientations by blue arrows. (c) The distribution of growth-cone alignment angles with respect to the nanoridge as a function of the growth-cone width. Darker to brighter colors indicate neuronal development stages from DIV 2 to DIV 8. (d) The average number of growth cones as a function of the alignment angle with respect to the nanoridges for early- and middle-stage neurons. Growth cones at angles between 0°and 15° are considered to be parallel, whereas growth cones at angles between 75° and 90° are considered to be perpendicular. (e) The relationship between the cross-sectional area and width of the growth cones, color-coded for developmental stage. Videos with at least one growth cone were considered for analysis. $N = 7$,

4, 1, 4, 3 for DIV 2, 3, 4, 7, and 8, respectively. Due to low *N*, we did not run statistical tests on the average number of growth cones across DIV stages and alignment angles.

We also observe that growth cones rarely adopt orientations around 45°, instead favoring directions either roughly parallel or perpendicular to the nanoridges (Fig. 5d). Although the fraction of parallel growth cones remains relatively stable from the early to the middle stage, the fraction of growth cones aligned perpendicularly increases substantially with development. These results suggest a potential shift in how neurons interact with the substrate over time. One possible interpretation is that at early stages, growth cones follow the nanoridges directly, as physical guides. As development proceeds, the surface becomes increasingly populated with existing neurites that span across multiple ridges, forming a complex internal landscape. New growth cones encountering this topography must navigate these pre-existing structures, leading to more perpendicular orientations as they fill in the gaps between ridge-aligned processes. This change could reflect a transition from external to internal guidance mechanisms, in which cell–cell interactions and tension along neurites begin to override substrate cues.

Finally, Fig. 5e shows that the growth-cone cross-sectional area is correlated positively with the growth-cone width. However, there is no significant change in either the area or the width of the growth cone as a function of developmental stage, suggesting that growth-cone are alone does not determine alignment or guidance behavior. Rather, it is the interplay between internal and external structural constraints that shapes the evolving trajectories of neurites.

## Discussion

We have characterized actin dynamics in primary rat cortical neurons at developmental stages ranging from DIV 2 (early) to DIV 23 (late), and have quantified these dynamics using an optical-flow based technique. Because primary cells have a finite lifetime *in vitro*, we focused on time points at which no degradation of the neural circuits was observed. Because actin dynamics can serve as a primary sensor of physical signals (22-24), we assessed how a well-established physical guidance cue, nanoridges, affects actin dynamics and neurite tips. Most previous studies (10, 11, 14, 41-43) used imaging frame rates on minute timescales, which are too slow to capture the actin polymerization waves that act as sensors of the physical environment. By imaging the dynamics of actin at a fast enough frame rate (0.5 frames/s), we are able to analyze how polymerization and depolymerization waves in primary neurons contribute to growth cone development, neuronal maturation, and sensing of the physical microenvironment.

We demonstrate that, on flat surfaces, the actin-wave speeds remain constant throughout neuronal development. In contrast, on nanoridges, actin-waves are suppressed, and the wave speed decreases slightly with increasing neuronal maturity. These findings suggest that actin is indeed functioning as a sensor of the environment, as our previous work in astrocytes found (24): when the environment is not as physiologically relevant (flat substrate of PDL-coated glass), actin wave speed does not change as neurons mature, but when the environment is more realistic (nanoridged substrate), actin wave speed decreases with neuronal maturity. Moreover, neurite orientation appears to be the primary guidance cue for the direction of actin-wave propagation throughout development. As neurons mature, the guidance of actin by nanoridges is reduced, and both neurite-tip and growth-cone guidance by nanoridges diminishes, with an increase in motion perpendicular to the nanoridges for actin waves, neurite tips, and growth cones.

Our findings demonstrate that the ability of neurons to sense and follow physical guidance cues may change with developmental stage, and raise the question of how such a change in physical sensing capabilities could impact brain development and regeneration. Recent studies have shown that promoting the physical microenvironment sensor of actin dynamics can enhance axon regeneration in the adult nervous system, particularly through the regulation of specific actin-binding proteins such as ADF/Cofilin (7). Understanding how nanotopography influences actin dynamics during various stages of development may thus provide valuable insights into potential strategies for promoting axon regeneration after injury or disease. It is important to note that our conclusions are limited to those that can be derived from an embryonic system, because even the “late stage” neurons in our study are still young compared to adult neurons in a living organism.

Finally, our findings may have implications for the development of novel therapeutic approaches for processes that are known to involve actin dynamics, in particular neuroregeneration (44),and the treatment of neurodegenerative diseases (45). Many studies have shown that brain stiffness decreases with age (46, 47) and that varying substrate stiffness affects neuronal morphology (48, 49). Thus our work provides a baseline for future studies investigating how to tune actin dynamics and thus neurite tip guidance to physical microenvironments that more closely mimic the brain at various developmental or disease stages.

## Acknowledgments

This work was supported by the US Air Force Office of Scientific Research MURI grant FA9550-16-1-0052 to W.L. and J.F. It was also supported in part by funds from the Intramural Research Program of NINDS, NIH: ZIA NS003013 to E.G.

## References

1. Ma L. Generation of Axons and Dendrites. In: Pfaff DW, Volkow ND, Rubenstein JL, editors. Neuroscience in the 21st Century: From Basic to Clinical. Cham: Springer International Publishing; 2022. p. 341-56.
2. Yogev S, Shen K. Establishing Neuronal Polarity with Environmental and Intrinsic Mechanisms. Neuron. 2017;96(3):638-50.
3. Nakajima C, Sawada M, Umeda E, Takagi Y, Nakashima N, Kuboyama K, et al. Identification of the growth cone as a probe and driver of neuronal migration in the injured brain. Nature Communications. 2024;15(1):1877.
4. Inagaki N, Katsuno H. Actin Waves: Origin of Cell Polarization and Migration? Trends Cell Biol. 2017;27(7):515-26.
5. Zhao B, Meka DP, Scharrenberg R, König T, Schwanke B, Kobler O, et al. Microtubules Modulate F-actin Dynamics during Neuronal Polarization. Scientific Reports. 2017;7(1):9583.
6. Cammarata GMaBEAaLLA. Cytoskeletal social networking in the growth cone: How +TIPs mediate microtubule-actin cross-linking to drive axon outgrowth and guidance. Cytoskeleton. 2016;73(9):461-76.
7. Leite SC, Pinto-Costa R, Sousa MM. Actin dynamics in the growth cone: a key player in axon regeneration. Curr Opin Neurobiol. 2021;69:11-8.

8. Marsh L, Letourneau PC. Growth of neurites without filopodial or lamellipodial activity in the presence of cytochalasin B. J Cell Biol. 1984;99(6):2041-7.
9. Bentley D, Toroian-Raymond A. Disoriented pathfinding by pioneer neurone growth cones deprived of filopodia by cytochalasin treatment. Nature. 1986;323(6090):712-5.
10. Clarke A, McQueen PG, Fang HY, Kannan R, Wang V, McCreedy E, et al. Dynamic morphogenesis of a pioneer axon in Drosophila and its regulation by Abl tyrosine kinase. Mol Biol Cell. 2020;31(6):452-65.
11. Clarke A, McQueen PG, Fang HY, Kannan R, Wang V, McCreedy E, et al. Abl signaling directs growth of a pioneer axon in Drosophila by shaping the intrinsic fluctuations of actin. Mol Biol Cell. 2020;31(6):466-77.
12. Ruthel G, Hollenbeck PJ. Growth cones are not required for initial establishment of polarity or differential axon branch growth in cultured hippocampal neurons. J Neurosci. 2000;20(6):2266-74.
13. Mortal S, Iseppon F, Perissinotto A, D'Este E, Cojoc D, Napolitano LMR, et al. Actin Waves Do Not Boost Neurite Outgrowth in the Early Stages of Neuron Maturation. Front Cell Neurosci. 2017;11:402.
14. Winans AM, Collins SR, Meyer T. Waves of actin and microtubule polymerization drive microtubule-based transport and neurite growth before single axon formation. Elife. 2016;5:e12387.
15. Hjorth JJ, van Pelt J, Mansvelder HD, van Ooyen A. Competitive dynamics during resource-driven neurite outgrowth. PLoS One. 2014;9(2):e86741.
16. Moore SW, Sheetz MP. Biophysics of substrate interaction: influence on neural motility, differentiation, and repair. Dev Neurobiol. 2011;71(11):1090-101.
17. Catherine V. Spatial confinement: A spur for axonal growth. Seminars in Cell & Developmental Biology. 2023;140:54-62.
18. Simitzi C, Ranella A, Stratakis E. Controlling the morphology and outgrowth of nerve and neuroglial cells: The effect of surface topography. Acta Biomaterialia. 2017;51:21-52.
19. Micholt L, Gärtner A, Prodanov D, Braeken D, Dotti CG, Bartic C. Substrate topography determines neuronal polarization and growth in vitro. PLoS One. 2013;8(6):e66170.
20. Vecchi JT, Rhomberg M, Guymon CA, Hansen MR. The geometry of photopolymerized topography influences neurite pathfinding by directing growth cone morphology and migration. J Neural Eng. 2024;21(2).
21. Yang Q, Miao Y, Campanello LJ, Hourwitz MJ, Abubaker-Sharif B, Bull AL, et al. Cortical waves mediate the cellular response to electric fields. eLife. 2022;11:e73198.
22. Bull AL, Mosher M, Rodriguez P, Fox S, Hourwitz MJ, Fourkas JT, et al. Suppressing collective cell motion with bidirectional guidance cues. Physical Review E. 2025;111(2):024409.
23. Yang Q, Miao Y, Banerjee P, Hourwitz MJ, Hu M, Qing Q, et al. Nanotopography modulates intracellular excitable systems through cytoskeleton actuation. Proceedings of the National Academy of Sciences. 2023;120(19):e2218906120.
24. O'Neill KM, Saracino E, Barile B, Mennona NJ, Mola MG, Pathak S, et al. Decoding Natural Astrocyte Rhythms: Dynamic Actin Waves Result from Environmental Sensing by Primary Rodent Astrocytes. Adv Biol (Weinh). 2023;7(6):e2200269.
25. Abdelrahman MH, Shen J, Fisher NC, Losert W, Fourkas JT. Assessing the stability of azopolymer nanotopography during live-cell fluorescence imaging. Frontiers in Bioengineering and Biotechnology. 2024;Volume 12 - 2024.
26. Sun X, Hourwitz MJ, Baker EM, Schmidt BUS, Losert W, Fourkas JT. Replication of biocompatible, nanotopographic surfaces. Sci Rep. 2018;8(1):564.
27. Schmid H, Michel B. Siloxane Polymers for High-Resolution, High-Accuracy Soft Lithography. Macromolecules. 2000;33(8):3042-9.
28. Simoncelli E. Design of multi-dimensional derivative filters. Proceedings of 1st IEEE International Conference on Image Processing; Austin, Texas1994. p. 790-3.

29. Lucas BD, Kanade T. An iterative image registration technique with an application to stereo vision | Proceedings of the 7th international joint conference on Artificial intelligence - Volume 2. Proceedings of the 7th International Joint Conference on Artificial Intelligence. 1981:pp 674-9.
30. Niblack W. An introduction to digital image processing: Strandberg Publishing Company; 1985.
31. Mennona NJ, Sedelnikova A, Echchgadda I, Losert W. Filament displacement image analytics tool for use in investigating dynamics of dense microtubule networks. Physical Review E. 2023;108(3):034411.
32. Lee RM, Campanello L, Hourwitz MJ, Alvarez P, Omidvar A, Fourkas JT, et al. Quantifying topography-guided actin dynamics across scales using optical flow. Mol Biol Cell. 2020;31(16):1753-64.
33. Vaserstein LN. Markov Processes over Denumerable Products of Spaces, Describing Large Systems of Automata. Probl Peredachi Inf. 1969;5(3):64-72.
34. Shapiro SS, Wilk MB. An Analysis of Variance Test for Normality (Complete Samples). Biometrika. 1965;52(3/4):591-611.
35. Tukey JW. Comparing Individual Means in the Analysis of Variance. Biometrics. 1949;5(2):99-114.
36. Kruskal WH, and Wallis WA. Use of Ranks in One-Criterion Variance Analysis. Journal of the American Statistical Association. 1952;47(260):583-621.
37. Dunn OJ. Multiple comparisons using rank sums. Technometrics. 1964;6(3):241-52.
38. Student. The Probable Error of a Mean. Biometrika. 1908;6(1):1-25.
39. Mann HB, Whitney DR. On a test of whether one of two random variables is stochastically larger than the other. Annals of Mathematical Statistics. 1947;18:50-60.
40. Qiao C, Zeng Y, Meng Q, Chen X, Chen H, Jiang T, et al. Zero-shot learning enables instant denoising and super-resolution in optical fluorescence microscopy. Nature Communications. 2024;15(1):4180.
41. San Miguel-Ruiz JE, Letourneau PC. The role of Arp2/3 in growth cone actin dynamics and guidance is substrate dependent. J Neurosci. 2014;34(17):5895-908.
42. Marsick BM, Flynn KC, Santiago-Medina M, Bamburg JR, Letourneau PC. Activation of ADF/cofilin mediates attractive growth cone turning toward nerve growth factor and netrin-1. Dev Neurobiol. 2010;70(8):565-88.
43. Suter DM, Forscher P. Substrate–cytoskeletal coupling as a mechanism for the regulation of growth cone motility and guidance. Journal of Neurobiology. 2000;44(2):97-113.
44. Blanquie O, Bradke F. Cytoskeleton dynamics in axon regeneration. Current Opinion in Neurobiology. 2018;51:60-9.
45. Bernstein BW, Maloney MT, Bamburg JR. Actin and Diseases of the Nervous System. Adv Neurobiol. 2011;5:201-34.
46. Arani A, Murphy MC, Glaser KJ, Manduca A, Lake DS, Kruse SA, et al. Measuring the effects of aging and sex on regional brain stiffness with MR elastography in healthy older adults. NeuroImage. 2015;111:59-64.
47. Takamura T, Motosugi U, Sasaki Y, Kakegawa T, Sato K, Glaser KJ, et al. Influence of Age on Global and Regional Brain Stiffness in Young and Middle-Aged Adults. Journal of Magnetic Resonance Imaging. 2020;51(3):727-33.
48. Previtera ML, Langhammer CG, Firestein BL. Effects of substrate stiffness and cell density on primary hippocampal cultures. J Biosci Bioeng. 2010;110(4):459-70.
49. Previtera ML, Langhammer CG, Langrana NA, Firestein BL. Regulation of dendrite arborization by substrate stiffness is mediated by glutamate receptors. Ann Biomed Eng. 2010;38(12):3733-43.